Available online at www.sciencedirect.com
SCIENCE DIRECT®
Journal of Computational Physics 213 (2006) 31–56
JOURNAL OF COMPUTATIONAL PHYSICS
www.elsevier.com/locate/jcp

Unified formulation for compressible and incompressible flows by using multi-integrated moments II: Multi-dimensional version for compressible and incompressible flows

Feng Xiao [a,b,*], Ryosuke Akoh [a], Satoshi Ii [a]

[a] Department of Energy Sciences, Tokyo Institute of Technology, 4259 Nagatsuta, Midori-ku, Yokohama 226-8502, Japan
[b] State Key Laboratory of Severe Weather, Chinese Academy of Meteorological Sciences, 46 Zhongguancun South Street, Beijing 100081, China

Received 3 February 2005; received in revised form 1 August 2005; accepted 1 August 2005
Available online 12 September 2005

Abstract

Following our previous paper on a novel finite volume formulation for computing flows of any Mach number, we present the multi-dimensional extension of the method in this paper. Treating two kinds of averages, which are generically called 'moments' and defined as the volume integrated average (VIA) and the surface integrated average (SIA) in this paper, as the prognostic variables makes the present method different from the conventional finite volume method where only VIA is the basic variable. The resulting discretization approach, which is a type of the CIP/multi-moment finite volume method and called VSIAM3 (volume/surface integrated average-based multi-moment method), is combined with a pressure-based projection formulation for the time integration to enable the simulations for both compressible and incompressible flows.

The numerical algorithm for multi-dimensions will be reported in this paper. Numerical experiments with flows of a wide range Mach numbers will be also presented.

AMS: 65P05; 77F05

MRI: 65C20; 76M20; 76T05

Keywords: Unified method; Conservative scheme; Multi-dimensional simulation; Pressure projection; Euler conservation laws; Shock capturing; Compressible and incompressible flows

DOI of original article: 10.1016/j.jcp.2003.10.014.
* Corresponding author. Tel./fax: +81 45 924 5538.
E-mail address: xiao@es.titech.ac.jp (F. Xiao).

0021-9991/$ - see front matter
doi:10.1016/j.jcp.2005.08.002

1. Introduction

Unified numerical formulation for all Mach numbers or for compressible and incompressible flows is very important in practical applications, especially where complex flows of a wide range Mach numbers are mixed. However, most of the existing fluid solvers are developed solely for either compressible or incompressible flows. There are some substantial barriers when one applies a scheme of one regime to a problem of another regime. For example, when using a density-based explicit method (see [18] for an extensive review of this type methods) to low Mach or incompressible flows, one has to deal with the singularity in the limit of small Mach number, which makes the pressure extremely sensitive to even a tiny change in density, and the severe restriction on the CFL condition of stability. On the other hand, when applying any of the pressure-based methods [3,6–9,12] to compressible or high Mach flows, one may have troubles in conservation and the poor resolutions of shock waves. Studies intending to bridge the gap of the two categories and to find numerical schemes that work well for all Mach flows have been so far carried out by either preconditioning the density-based explicit methods [5,13,19,20,22] or improving the numerical accuracy of pressure-based semi-implicit methods [1,10,11,15,16,30]. The resulting schemes are usually called unified methods. See [23] for a more complete review.

In the previous paper [24], a one-dimensional finite volume method for arbitrary Mach number flows is presented by employing a pressure-based projection method and a novel spatial discretization formulation that uses both the cell-integrated average and the interface value as the model variables. In three-dimensional case, the cell-integrated average and the interface value are correspondingly defined as the volume integrated average (VIA) and the surface integrated average (SIA). All these quantities are generically called 'moments' in our context. The basic idea of the spatial discretization comes from the underlying concept of the CIP (cubic interpolated propagation or constrained interpolation profile) method [28,31], i.e., making use more than one moments as the model variables in computational models. The resulting discretization formulation, namely VSIAM3 (volume/surface integrated average-based multi-moment method), is different from the traditional finite volume method where only the volume averaged values are treated as the model variables. Incorporating the VSIAM3 with a projection scheme leads to a convenient algorithm to compute the compressible flows via a pressure-based numerical framework which was originally designed and has been so far widely used in the computations of incompressible flows. Shown in [24], the VSIAM3 gives satisfactory numerical results to various benchmark tests of the Euler conservation law, and appears to be promising in regard to numerical accuracy, robustness and algorithmic simplicity.

When extending the VSIAM3 to multi-dimensions, extra attention needs to be paid for updating the moments for all physical variables because multi-moments (two as VIA and SIA) are used as the dependent variables. In this paper, we present a simple multi-dimensional version for the VSIAM3. The multi-dimensional advection is computed by the CIP-CSL3 scheme [26], while the pressure projection and the viscous terms are computed by a fully multi-dimensional formulation based on VIA and SIAs of the physical variables.

In Section 2, the numerical formulations are described. The solution procedure using a pressure-based projection is similar to the 1D case reported in [24]. The multi-dimensional discretization of VSIAM3 will be presented in detail. Numerical tests are given in Section 3. With the 1D method extensively tested with various compressible flows in [24], some 2D numerical experiments of compressible and nearly incompressible flows will be presented to show the capability of the presented method as a unified solver in simulating different flows from highly compressible to nearly incompressible. The paper ends with some short remarks in Section 4.

2. Numerical formulations

2.1. Governing equations and fractional step procedure

We consider the following general conservation laws for per volume fluid in 2D:

$$\frac{\partial \rho}{\partial t} + \nabla \cdot \mathbf{m} = 0, \tag{1}$$

$$\frac{\partial \mathbf{m}}{\partial t} + \nabla \cdot (\mathbf{m} \otimes \mathbf{u}) = -\nabla p + \nabla \cdot \mathscr{T}, \tag{2}$$

$$\frac{\partial E}{\partial t} + \nabla \cdot (\mathbf{u}E) = -\nabla \cdot (p\mathbf{u}) + \nabla \cdot (\mathscr{T} \otimes \mathbf{u}), \tag{3}$$

where ρ is the density, $\mathbf{u} = (u_x, u_y) = (u, v)$ the velocity vector, $\mathbf{m} = (m_x, m_y) = (\rho u, \rho v)$ the momentum vector, p the pressure, E the total energy. Suppose we have perfect gas, the pressure can be obtained by the equation of state as $p = (E - \rho u^2/2)(\gamma - 1)$ with γ being the ratio of the specific heats. Under the assumption of Newtonian fluid, the components of the viscous shear stress tensor $\mathscr{T}$ are evaluated as

$$\tau_{\alpha\beta} = \mu\left[\left(\frac{\partial u_\alpha}{\partial \beta} + \frac{\partial u_\beta}{\partial \alpha}\right) - \frac{2}{3}(\nabla \cdot \mathbf{u})\hat{\delta}_{\alpha\beta}\right] \quad \text{with } \alpha, \beta = x, y, \tag{4}$$

where μ is the dynamic viscosity of the fluid, and $\hat{\delta}_{\alpha\beta}$ is the Kronecker delta.

As discussed in [23], when the flow is of small Mach number or incompressible, singularity arises from the process of obtaining the pressure with the equation of state after ρ and E are computed as the dependent variables. As a remedy to this, the equation of the total energy can be replaced by a prognostic equation of pressure which then can be solved simultaneously with the continuity equation and the momentum equation in an implicit way for the low Mach flow. Among others, the examples of this type treatment are found in [1,21,30]. In [24], we retain the conservative equation for the total energy, but update the pressure through a semi-implicit step in the non-advection phase, which works as the pressure-based projection when the flow becomes incompressible. Similar to the 1D version in [24], we briefly describe the solution procedure supposing that we know all values at nth step as ρ^n, $\mathbf{m}^n$ and E^n.

Adopting a fractional step approach, we first compute the advection part (i.e., the left-hand side of Eqs. (1)–(3)) with the CIP-CSL3 scheme [26], whose multi-dimensional implementation is going to be described later, and obtain the value for density at the new time step ρ^{n+1} and the provisional values of the momentum and the total energy as $\mathbf{m}^{\diamondsuit}$ and $E^{\diamondsuit}$. Similar to the 1D case, the semi-discretized equations of the non-advection part are then written as

$$\frac{\mathbf{m}^{n+1} - \mathbf{m}^{\diamondsuit}}{\Delta t} = -\nabla p^{n+1} \tag{5}$$

and

$$\frac{E^{n+1} - E^{\diamondsuit}}{\Delta t} = -\nabla \cdot (\mathbf{u}p)^{n+1}, \tag{6}$$

where Δt is the time integration interval. Note that we have omitted the sub-steps for viscous and source terms for forcing and heating, which can be included by just adding extra sub-steps for the corresponding physics after the advection computation. The updated values are then superscripted with $^{\diamondsuit}$ and used in the following projection procedure.

From (5), we have

$$\frac{1}{\Delta t}\left(\nabla\cdot\mathbf{m}^{n+1}-\nabla\cdot\mathbf{m}^{\diamondsuit}\right)=-\nabla^2 p^{n+1}. \tag{7}$$

The first term on the left-hand side of Eq. (7) provides an interface to include the compressibility into a pressure-based projection method, and is approximated by

$$\nabla\cdot\mathbf{m}^{n+1}=\mathbf{u}^{\diamondsuit}\cdot\nabla\rho^{n+1}+\rho^{n+1}\nabla\cdot\mathbf{u}^{n+1}. \tag{8}$$

For compressible flow, change in fluid density connects directly to the volume change rate, hence to the divergence which is then expressed through the spatial variations in velocity. This is presented by the following equation:

$$\frac{\delta\rho}{\delta t}=-\rho\nabla\cdot\mathbf{u}, \tag{9}$$

where $\delta/\delta t$ and $\nabla\cdot\mathbf{u}$ denote the variations in time and volume change rate for a fluid parcel.

Recall the equation of state and the first law of thermodynamics, we have the following relations among the thermodynamic variables and the velocity field.

$$\frac{\delta p}{\delta t}=(\gamma-1)\left(e\frac{\delta\rho}{\delta t}+\rho\frac{\delta e}{\delta t}\right), \tag{10}$$

where e is the internal energy, and

$$\frac{\delta e}{\delta t}=-\frac{p}{\rho}\nabla\cdot\mathbf{u}. \tag{11}$$

Eqs. (9)–(11) are the part that relates to the acoustic wave and compressibility. We then arrive at

$$\nabla\cdot\mathbf{u}=-\frac{1}{\gamma p}\frac{\delta p}{\delta t}. \tag{12}$$

The above relation states the response of the velocity field to the disturbance in the pressure field or vice versa.

By replacing the divergence term expressed by (12) in (8) and using Euler forward stepping to the pressure tendency, we recast (7) as

$$\nabla^2 p^{n+1}=\frac{1}{\Delta t}\left(-\mathbf{u}^{\diamondsuit}\cdot\nabla\rho^{n+1}+\frac{1}{C^2}\frac{p^{n+1}-p^{\diamondsuit}}{\Delta t}+\nabla\cdot\mathbf{m}^{\diamondsuit}\right), \tag{13}$$

where $C=\sqrt{\gamma p^{\diamondsuit}/\rho^{n+1}}$ is the sound speed, and the intermediate pressure is computed by $p^{\diamondsuit}=(E^{\diamondsuit}-\rho^{n+1}(\mathbf{u}^{\diamondsuit})^2/2)(\gamma-1)$.

Rewriting Eq. (13) as

$$\left(-\frac{1}{C^2\Delta t}+\nabla^2\right)p^{n+1}=\frac{1}{\Delta t}\left(-\mathbf{u}^{\diamondsuit}\cdot\nabla\rho^{n+1}+\frac{-\rho^{n+1}}{\gamma\Delta t}+\nabla\cdot\mathbf{m}^{\diamondsuit}\right), \tag{14}$$

we find that by updating pressure from the Poisson equation (14), we avoid the singularity in the process of computing pressure from density and internal energy through equation of state. It is also obvious that Eq. (13) becomes exactly the pressure Poisson equation in the projection method for incompressible flows when the sound speed C becomes infinite or the Mach number ($M=u/C$) approaches zero.

Poisson pressure equation (14) can be solved by any standard iterative method. After p^{n+1} is solved from (14), the momentum and the total energy are then updated by (5) and (6). It is noted that all the mass,

momentum and total energy are predicted in a conservative form, which is different from those reported in [1,30] where all or part of the variables are computed by non-conservative formulations. Using multi-integrated moments, our spatial discretizations for the above equations are different from the conventional finite difference method or finite volume method, and will be discussed next.

2.2. Spatial discretization in multi-dimensions

The multi-dimensional discretization of VSIAM3 is a straightforward extension of its 1D version in [24]. An implementation of VSIAM3 to incompressible flow can be found in [25]. We include the two-dimensional formulation below for the completeness of the present paper.

In VSIAM3, the model variables are the VIA and SIAs for each time-evolution physical variable. We denote VIA and SIA of physical variable $\phi(x,y,t)$ by $\overline{^{V}\phi}$, $\overline{^{S^x}\phi}$ and $\overline{^{S^y}\phi}$ in 2D Cartesian grid (x,y).

In a Cartesian coordinate, the control volume is defined by a volume element (VE) $V_{ij} = [x_i - \frac{1}{2}, x_i + \frac{1}{2}] \times [y_j - \frac{1}{2}, y_j + \frac{1}{2}]$ and four surface elements (SE) $S^x_{i\pm\frac{1}{2}j} = x_{i\pm\frac{1}{2}} \cap [y_{j-\frac{1}{2}}, y_{j+\frac{1}{2}}]$, $S^y_{ij\pm\frac{1}{2}} = y_{j\pm\frac{1}{2}} \cap [x_{i-\frac{1}{2}}, x_{i+\frac{1}{2}}]$, as shown in Fig. 1.

The volume of the VE is consequently $|V_{ij}| = \Delta x_i \Delta y_j$, and the lengths of the SEs are $|S^x_{i\pm\frac{1}{2}j}| = \Delta y_j$ and $|S^y_{ij\pm\frac{1}{2}}| = \Delta x_i$, where $\Delta x_i = x_{i+\frac{1}{2}} - x_{i-\frac{1}{2}}$ and $\Delta y_j = y_{j+\frac{1}{2}} - y_{j-\frac{1}{2}}$.

The VIA and the SIAs of physical variable $\phi(x,y,t)$ are, respectively, defined on V_{ij}, $S^x_{i+\frac{1}{2}j}$ and $S^y_{ij+\frac{1}{2}}$ for all mesh cells by

$$\overline{^{V}\phi}_{ij} = \frac{1}{|V_{ij}|} \int_{x_{i-\frac{1}{2}}}^{x_{i+\frac{1}{2}}} \int_{y_{j-\frac{1}{2}}}^{y_{j+\frac{1}{2}}} \phi(x,y,t)\,\mathrm{d}x\,\mathrm{d}y, \tag{15}$$

$$\overline{^{S^x}\phi}_{i+\frac{1}{2}j} = \frac{1}{|S^x_{i+\frac{1}{2}j}|} \int_{y_{j-\frac{1}{2}}}^{y_{j+\frac{1}{2}}} \phi(x_{i+\frac{1}{2}},y,t)\,\mathrm{d}y \tag{16}$$

and

$$\overline{^{S^y}\phi}_{ij+\frac{1}{2}} = \frac{1}{|S^y_{ij+\frac{1}{2}}|} \int_{x_{i-\frac{1}{2}}}^{x_{i+\frac{1}{2}}} \phi(x,y_{j+\frac{1}{2}},t)\,\mathrm{d}x. \tag{17}$$

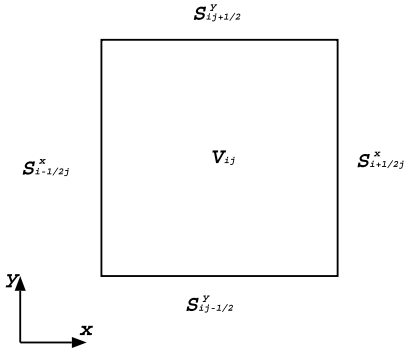

Fig. 1. A 2D control volume. VIA is defined on the volume elements (V_{ij}), while the SIAs are defined on the surface elements ($S^x_{i\pm\frac{1}{2}j}$, $S^y_{ij\pm\frac{1}{2}}$).

The discretization of the differential or integral operators can be computed using interpolations based on VIA and SIAs. Without losing generality, we consider the one-dimensional interpolation in x direction. A simple linear interpolation, for example, can be constructed by using the VIAs of two neighboring cells as

$$\Phi_1(x) = a_1 + b_1(x - x_{i+\frac{1}{2}}) \tag{18}$$

with

$$a_1 = \frac{1}{\Delta x_i + \Delta x_{i+1}}(\Delta x_{i+1}\overline{{}^{V}\phi}_{ij} + \Delta x_i \overline{{}^{V}\phi}_{i+1j}), \tag{19}$$

$$b_1 = \frac{2}{\Delta x_i + \Delta x_{i+1}}(\overline{{}^{V}\phi}_{i+1j} - \overline{{}^{V}\phi}_{ij}), \tag{20}$$

while a parabolic polynomial can be constructed by using both the VIA and SIA as

$$\Phi_2(x) = a_2 + b_2(x - x_{i+\frac{1}{2}}) + c_2(x - x_{i+\frac{1}{2}})^2, \tag{21}$$

where

$$a_2 = \overline{{}^{S^x}\phi}_{i+\frac{1}{2}j}, \tag{22}$$

$$b_2 = \frac{2}{\Delta x_i + \Delta x_{i+1}}\left[\frac{\Delta x_i}{\Delta x_{i+1}}(\overline{{}^{V}\phi}_{i+1j} - \overline{{}^{S^x}\phi}_{i+\frac{1}{2}j}) - \frac{\Delta x_{i+1}}{\Delta x_i}(\overline{{}^{V}\phi}_{ij} - \overline{{}^{S^x}\phi}_{i+\frac{1}{2}j})\right], \tag{23}$$

$$c_2 = 3\left[\frac{1}{\Delta x_i(\Delta x_i + \Delta x_{i+1})}(\overline{{}^{V}\phi}_{ij} - \overline{{}^{S^x}\phi}_{i+\frac{1}{2}j}) + \frac{1}{\Delta x_{i+1}(\Delta x_i + \Delta x_{i+1})}(\overline{{}^{V}\phi}_{i+1j} - \overline{{}^{S^x}\phi}_{i+\frac{1}{2}j})\right]. \tag{24}$$

The gradient operator at $S^x_{i+\frac{1}{2}j}$ then can be computed by

$$\overline{{}^{S^x}\partial_x\phi(x)}_{i+\frac{1}{2}j} = \left[\frac{\partial\Phi_1(x)}{\partial x}\right]_{i+\frac{1}{2}j} = b_1 \tag{25}$$

or

$$\overline{{}^{S^x}\partial_x\phi(x)}_{i+\frac{1}{2}j} = \left[\frac{\partial\Phi_2(x)}{\partial x}\right]_{i+\frac{1}{2}j} = b_2. \tag{26}$$

It is found that for constant grid spacing both (25) and (26) become the simple central differencing based on the two neighboring VIA values.

The Laplacian operator on V_{ij} can be approximated by

$$\overline{{}^{V}\partial_{xx}\phi(x)}_{ij} = \frac{1}{\Delta x_i}[\overline{{}^{S^x}\partial_x\phi(x)}_{i+\frac{1}{2}j} - \overline{{}^{S^x}\partial_x\phi(x)}_{i-\frac{1}{2}j}]. \tag{27}$$

The corresponding expressions in y direction can also be derived analogously.

Compared to the conventional FVM, in addition to VIA, the extra SIAs also need to be updated in a VSIAM3 model. The computation will become much heavier if we predict each SIA exactly according to the governing equations. Alternatively, a more efficient formulation can be constructed by solving parts of VIAs or SIAs, and then update the rest using the so-called TEC (time-evolution converting) formula with the time variation of either $(\frac{\delta\overline{{}^{V}\phi}}{\delta t})$ or $(\frac{\delta\overline{{}^{S^\alpha}\phi}}{\delta t})$ (for $\alpha = x, y$) known. A TEC formula is used to link the time variation between VIA and SIA, thus is in fact equivalent to the interpolation of operators. For example, a

simple linear interpolation leads to a second-order TEC that converts the time variation from VIA to SIA as

$$\delta_t \overline{{}^{Sx}\phi}_{i+\frac{1}{2}j} = \frac{1}{2}(\delta_t \overline{{}^{V}\phi}_{i+1j} + \delta_t \overline{{}^{V}\phi}_{ij}) \tag{28}$$

and one that converts the time variation from SIA to VIA as

$$\delta_t \overline{{}^{V}\phi}_{ij} = \frac{1}{2}(\delta_t \overline{{}^{Sx}\phi}_{i-\frac{1}{2}j} + \delta_t \overline{{}^{Sx}\phi}_{i+\frac{1}{2}j}). \tag{29}$$

A fourth-order explicit TEC foumulae on a uniform spaced mesh reads

$$\delta_t \overline{{}^{Sx}\phi}_{i+\frac{1}{2}j} = \frac{1}{12}[7(\delta_t \overline{{}^{V}\phi}_{i+1j} + \delta_t \overline{{}^{V}\phi}_{ij}) - (\delta_t \overline{{}^{V}\phi}_{i-1j} + \delta_t \overline{{}^{V}\phi}_{i+2j})], \tag{30}$$

or

$$\delta_t \overline{{}^{V}\phi}_{ij} = \frac{1}{24}[13(\delta_t \overline{{}^{Sx}\phi}_{i-\frac{1}{2}j} + \delta_t \overline{{}^{Sx}\phi}_{i+\frac{1}{2}j}) - (\delta_t \overline{{}^{Sx}\phi}_{i-\frac{3}{2}j} + \delta_t \overline{{}^{Sx}\phi}_{i+\frac{3}{2}j})]. \tag{31}$$

Using the TEC formula, we usually need to compute the governing equation of either VIA or SIA for only once. So, the increase of the computational efforts due to using multi-integrated moments is not significant.

Before going further for the description of the spatial discretization for the governing equations, we assume a constant grid spacing in both directions for simplicity and define the following notations.

- The subscript indexes of surface elements

$$\phi_{I_x} = \phi_{i+\frac{1}{2}j}, \quad \phi_{I_y} = \phi_{ij+\frac{1}{2}}.$$

- The difference operator

$$\delta_x(\phi)_{ij} = \frac{1}{\Delta x_i}(\phi_{i+\frac{1}{2}j} - \phi_{i-\frac{1}{2}j}), \quad \delta_y(\phi)_{ij} = \frac{1}{\Delta y_j}(\phi_{ij+\frac{1}{2}} - \phi_{ij-\frac{1}{2}}).$$

- The averaging operator

$$\overline{(\phi)}^{x}_{ij} = \frac{1}{2}(\phi_{i+\frac{1}{2}j} + \phi_{i-\frac{1}{2}j}), \quad \overline{(\phi)}^{y}_{ij} = \frac{1}{2}(\phi_{ij+\frac{1}{2}} + \phi_{ij-\frac{1}{2}}),$$
$$\overline{(\phi)}^{x}_{i+\frac{1}{2}j} = \frac{1}{2}(\phi_{i+1j} + \phi_{ij}), \quad \overline{(\phi)}^{y}_{ij+\frac{1}{2}} = \frac{1}{2}(\phi_{ij+1} + \phi_{ij}).$$

The divergence for control volume V_{ij} is computed via the SIAs of the velocity components normal to each surface element,

$$\mathscr{D}_{ij} = \delta_x(\overline{{}^{Sx}u})_{ij} + \delta_y(\overline{{}^{Sy}v})_{ij}. \tag{32}$$

2.3. Multi-dimensional implementation of CIP-CSL3 scheme

In the present model the advection computation can be solved by one of the CIP-CSL type schemes [26,27,29].

Concerning the multi-dimensional implementation of a CIP-CSL scheme, an efficient algorithm was devised based on just two integrated moments, i.e., the VIA and the SIA in [27].

In terms of VIA and SIA, the multi-dimensional advection scheme can be constructed through a simple splitting [27] based on a one-dimensional CIP-CSL scheme.

We consider the following 2D advection equation:

$$\frac{\partial \phi}{\partial t} + \frac{\partial (u\phi)}{\partial x} + \frac{\partial (v\phi)}{\partial y} = 0, \tag{33}$$

where ϕ is the transported quantity. The 2D CIP-CSL scheme in terms of VIA and SIA is devised to solve the VIA ($\overline{{}^{V}\phi}$) and the SIAs ($\overline{{}^{S^x}\phi}$ and $\overline{{}^{S^y}\phi}$) according to the following semi-discretized equations:

$$\frac{\partial \overline{{}^{V}\phi}_{ij}}{\partial t} + \delta_x[\mathscr{F}_x(\overline{{}^{S^x}u}, \overline{{}^{S^x}\phi}, \overline{{}^{V}\phi})]_{ij} + \delta_y[\mathscr{F}_y(\overline{{}^{S^y}v}, \overline{{}^{S^y}\phi}, \overline{{}^{V}\phi})]_{ij} = 0 \tag{34}$$

and

$$\frac{\mathrm{d}\overline{{}^{S^\alpha}\phi}_{I_\alpha}}{\mathrm{d}t} + \overline{(\overline{{}^{V}\phi}\mathscr{D})}^{\alpha}_{I_\alpha} = 0 \quad \text{with } \alpha = x, y, \tag{35}$$

where $\mathscr{F}_x(\overline{{}^{S^x}u}, \overline{{}^{S^x}\phi}, \overline{{}^{V}\phi})$ and $\mathscr{F}_y(\overline{{}^{S^y}v}, \overline{{}^{S^y}\phi}, \overline{{}^{V}\phi})$ represent the advection fluxes in x and y directions, respectively. $\mathrm{d}/\mathrm{d}t$ is the substantial derivative. The advection velocity components denoted by $\overline{{}^{S^x}u}$ and $\overline{{}^{S^y}v}$ are the SIAs of the normal components of velocity in each direction. In the CIP-CSL3 scheme, a cubic interpolation function is constructed by using both VIA and SIA of the transported quantity. The VIA value is then computed by a flux-based formulation, while the substantial derivative of the SIA in Eq. (35) is at first updated by a semi-Lagrangian step and then corrected by an extra step that evaluates the divergence term along the foot trajectory. See [26] for more details.

Using splitting, a simple two-dimensional algorithm on a uniform grid reads as follows:

Given VIA and SIAs ($\overline{{}^{V}\phi}^{n}_{ij}$, $\overline{{}^{S^x}\phi}^{n}_{i+\frac{1}{2}j}$ and $\overline{{}^{S^y}\phi}^{n}_{ij+\frac{1}{2}}$) at the nth step.

x direction:

x1: compute $\overline{{}^{V}\phi}^{*}_{ij}$, $\overline{{}^{S^x}\phi}^{*}_{i+\frac{1}{2}j}$ from $\overline{{}^{V}\phi}^{n}_{ij}$, $\overline{{}^{S^x}\phi}^{n}_{i+\frac{1}{2}j}$ with the 1D scheme.

x2: update $\overline{{}^{S^y}\phi}^{*}_{ij+\frac{1}{2}}$ by the time evolution converting (TEC) formula in y direction as

$$\overline{{}^{S^y}\phi}^{*}_{ij+\frac{1}{2}} = \overline{{}^{S^y}\phi}^{n}_{ij+\frac{1}{2}} + \frac{1}{2}(\overline{{}^{V}\phi}^{*}_{ij+1} - \overline{{}^{V}\phi}^{n}_{ij+1} + \overline{{}^{V}\phi}^{*}_{ij} - \overline{{}^{V}\phi}^{n}_{ij}).$$

y direction:

y1: compute $\overline{{}^{V}\phi}^{\diamondsuit}_{ij}$, $\overline{{}^{S^y}\phi}^{\diamondsuit}_{ij+\frac{1}{2}}$ from $\overline{{}^{V}\phi}^{*}_{ij}$, $\overline{{}^{S^y}\phi}^{*}_{ij+\frac{1}{2}}$ with the 1D scheme.

y2: similar to step *x2*, update $\overline{{}^{S^x}\phi}^{\diamondsuit}_{i+\frac{1}{2}j}$ by TEC formula in x direction as

$$\overline{{}^{S^x}\phi}^{\diamondsuit}_{i+\frac{1}{2}j} = \overline{{}^{S^x}\phi}^{*}_{i+\frac{1}{2}j} + \frac{1}{2}(\overline{{}^{V}\phi}^{\diamondsuit}_{i+1j} - \overline{{}^{V}\phi}^{*}_{i+1j} + \overline{{}^{V}\phi}^{\diamondsuit}_{ij} - \overline{{}^{V}\phi}^{*}_{ij}).$$

In steps *x2* and *y2*, the TEC formula is an interpolation approximation for time derivative. Given in the above expressions are just the linear interpolation. As shown before, higher order explicit approximations or splines can also be used. The correction to the dimensional splitting as discussed in [2] is added to remedy the splitting errors from a variable velocity field.

It is noted that the flux formulation used to compute the VIA in the CIP-CSL3 scheme assures the conservation. As in [24], the CIP-CSL3 scheme provides a device in the interpolation reconstruction to control both the numerical oscillation and the numerical diffusion.

2.4. Discretization of the governing equations

As discussed above, with the spatial discretization constructed in terms of VIAs and SIAs, the corresponding semi-discretized expressions for the governing equations (1)–(3) are written as follows:

Continuity equation

$$\frac{\partial \overline{{}^{V}\rho_{ij}}}{\partial t} + \delta_x[\mathscr{F}_x(\overline{{}^{S^x}u}, \overline{{}^{S^x}\rho}, \overline{{}^{V}\rho})]_{ij} + \delta_y[\mathscr{F}_y(\overline{{}^{S^y}v}, \overline{{}^{S^y}\rho}, \overline{{}^{V}\rho})]_{ij} = 0, \tag{36}$$

$$\frac{\mathrm{d}\overline{{}^{S^\alpha}\rho_{I_\alpha}}}{\mathrm{d}t} + \overline{(\overline{{}^{V}\rho}\mathscr{D})}^{\alpha}_{I_\alpha} = 0 \quad \text{with } \alpha = x, y. \tag{37}$$

Momentum equation

$$\frac{\partial \overline{{}^{V}m_{xij}}}{\partial t} + \delta_x[\mathscr{F}_x(\overline{{}^{S^x}u}, \overline{{}^{S^x}m_x}, \overline{{}^{V}m_x})]_{ij} + \delta_y[\mathscr{F}_y(\overline{{}^{S^y}v}, \overline{{}^{S^y}m_x}, \overline{{}^{V}m_x})]_{ij} = -\overline{(\overline{{}^{S^x}\partial_x p})}^{x}_{ij} + \mathscr{T}_{xij}, \tag{38}$$

$$\frac{\mathrm{d}\overline{{}^{S^x}m_x}_{i+\frac{1}{2}j}}{\mathrm{d}t} + \overline{(\overline{{}^{V}m_x}\mathscr{D})}^{x}_{i+\frac{1}{2}j} = -\overline{{}^{S^x}\partial_x p}_{i+\frac{1}{2}j} + \overline{(\mathscr{T}_x)}^{x}_{i+\frac{1}{2}j}, \tag{39}$$

$$\frac{\mathrm{d}\overline{{}^{S^y}m_x}_{ij+\frac{1}{2}}}{\mathrm{d}t} + \overline{(\overline{{}^{V}m_x}\mathscr{D})}^{y}_{ij+\frac{1}{2}} = -\overline{[\overline{(\overline{{}^{S^x}\partial_x p})}^{x}]}^{y}_{ij+\frac{1}{2}} + \overline{(\mathscr{T}_x)}^{y}_{ij+\frac{1}{2}}, \tag{40}$$

$$\frac{\partial \overline{{}^{V}m_{yij}}}{\partial t} + \delta_x[\mathscr{F}_x(\overline{{}^{S^x}u}, \overline{{}^{S^x}m_y}, \overline{{}^{V}m_y})]_{ij} + \delta_y[\mathscr{F}_y(\overline{{}^{S^y}v}, \overline{{}^{S^y}m_y}, \overline{{}^{V}m_y})]_{ij} = -\overline{(\overline{{}^{S^y}\partial_y p})}^{y}_{ij} + \mathscr{T}_{yij}, \tag{41}$$

$$\frac{\mathrm{d}\overline{{}^{S^y}m_y}_{ij+\frac{1}{2}}}{\mathrm{d}t} + \overline{(\overline{{}^{V}m_y}\mathscr{D})}^{y}_{ij+\frac{1}{2}} = -\overline{{}^{S^y}\partial_y p}_{ij+\frac{1}{2}} + \overline{(\mathscr{T}_y)}^{y}_{ij+\frac{1}{2}}, \tag{42}$$

$$\frac{\mathrm{d}\overline{{}^{S^x}m_y}_{i+\frac{1}{2}j}}{\mathrm{d}t} + \overline{(\overline{{}^{V}m_y}\mathscr{D})}^{x}_{i+\frac{1}{2}j} = -\overline{[\overline{(\overline{{}^{S^y}\partial_y p})}^{y}]}^{x}_{i+\frac{1}{2}j} + \overline{(\mathscr{T}_y)}^{x}_{i+\frac{1}{2}j}. \tag{43}$$

Energy equation

$$\begin{aligned}&\frac{\partial \overline{{}^{V}E_{ij}}}{\partial t} + \delta_x[\mathscr{F}_x(\overline{{}^{S^x}u}, \overline{{}^{S^x}E}, \overline{{}^{V}E})]_{ij} + \delta_y[\mathscr{F}_y(\overline{{}^{S^y}v}, \overline{{}^{S^y}E}, \overline{{}^{V}E})]_{ij} \\ &\quad = -[\delta_x(\overline{{}^{S^x}up})_{ij} + \delta_y(\overline{{}^{S^y}vp})_{ij}] + \delta_x(\overline{{}^{S^x}u\mathscr{T}_x})_{ij} + \delta_y(\overline{{}^{S^y}v\mathscr{T}_y})_{ij},\end{aligned} \tag{44}$$

$$\frac{\mathrm{d}\overline{{}^{S^\alpha}E_{I_\alpha}}}{\mathrm{d}t} + \overline{(\overline{{}^{V}E}\mathscr{D})}^{\alpha}_{I_\alpha} = -\overline{[\delta_x(\overline{{}^{S^x}up}) + \delta_y(\overline{{}^{S^y}vp})]}^{\alpha}_{I_\alpha} + \overline{[\delta_x(\overline{{}^{S^x}u\mathscr{T}_x})]}^{\alpha}_{I_\alpha} + \overline{[\delta_y(\overline{{}^{S^y}v\mathscr{T}_y})]}^{\alpha}_{I_\alpha} \quad \text{with } \alpha = x, y. \tag{45}$$

The gradient forces of the viscous stress are computed as

$$\mathscr{T}_{\alpha ij} = \sum_{\beta=x,y} \delta_\beta(\overline{{}^{S^\beta}\tau_{\alpha\beta}})_{ij} \quad \text{with } \alpha = x, y. \tag{46}$$

The advections are sorted on the left-hand side of Eqs. (36)–(45) and solved by the CIP-CSL3 scheme. The spatial discretizations in the above equations are constructed by using both the VIAs and the SIAs of the physical variables.

As mentioned earlier, the averagings of operators are equivalent to the TEC formula that convert the temporal changes between VIA and SIA for the corresponding physical variable. For example, given the VIA of any physical variable being updated by the discretized governing equation due to operator $\Psi(\phi)$ as

$$\delta_t^{\Psi}\overline{{}^{V}\phi}_{ij} \equiv \frac{\delta^{\Psi}\overline{{}^{V}\phi}_{ij}}{\delta t} = \Psi(\overline{{}^{V}\phi}, \overline{{}^{S^x}\phi}, \overline{{}^{S^y}\phi}), \tag{47}$$

the computation of SIA $\overline{{}^{S^\alpha}\phi}_{I_\alpha}$ expressed by

$$\frac{\delta\overline{{}^{S^\alpha}\phi}^{\Psi}_{I_\alpha}}{\delta t} = \overline{\Psi(\overline{{}^{V}\phi}, \overline{{}^{S^x}\phi}, \overline{{}^{S^y}\phi})}^{\alpha}_{I_\alpha}, \quad \alpha = x, y; \tag{48}$$

in (36)–(45) can be simply computed by the TEC formula as

$$\overline{{}^{S^x}\phi}^{\Psi}_{i+\frac{1}{2}j} = \overline{{}^{S^x}\phi}_{i+\frac{1}{2}j} + \delta_t^{\Psi}(\overline{{}^{S^x}\phi}_{i+\frac{1}{2}j})\Delta t = \overline{{}^{S^x}\phi}_{i+\frac{1}{2}j} + \frac{1}{2}(\delta_t^{\Psi}\overline{{}^{V}\phi}_{i+1j} + \delta_t^{\Psi}\overline{{}^{V}\phi}_{ij})\Delta t, \tag{49}$$

$$\overline{{}^{S^y}\phi}^{\Psi}_{ij+\frac{1}{2}} = \overline{{}^{S^y}\phi}_{ij+\frac{1}{2}} + \delta_t^{\Psi}(\overline{{}^{S^y}\phi}_{ij+\frac{1}{2}})\Delta t = \overline{{}^{S^y}\phi}_{ij+\frac{1}{2}} + \frac{1}{2}(\delta_t^{\Psi}\overline{{}^{V}\phi}_{ij+1} + \delta_t^{\Psi}\overline{{}^{V}\phi}_{ij})\Delta t. \tag{50}$$

In the above expressions, ϕ^{Ψ} denotes the renewed value due to the contribution of operator Ψ and δ_t^{Ψ} the corresponding time increment. We further denote the computations of (49) and (50) by $\overline{{}^{S^\alpha}\phi}_{I_\alpha} \overset{\text{TEC}}{\rightarrow} \overline{{}^{S^\alpha}\phi}^{\Psi}_{I_\alpha}$.

We should remark that the TEC formula like (49) and (50) is computationally stable only if the scheme for updating the VIA in (47) is stable. This is a straightforward conclusion from the fact that a bounded interpolation or averaging of the numerical errors from a stable scheme always results in bounded errors.

Simple arithmetic averages as (49) and (50) are used in the numerical tests reported in this paper.

2.5. The solution procedure

The time integration procedure for each step which updates all physical variables from step n ($t = t^n$) to step $n+1$ ($t = t^{n+1} = t^n + \Delta t$) is summarized as follows:

(i) Compute the advection phase by the CIP-CSL3 scheme and get the provisional values for the VIAs ($\overline{{}^{V}\phi}^{\diamondsuit}$) and the SIAs ($\overline{{}^{S^\alpha}\phi}^{\diamondsuit}$ for $\alpha = x, y$). At this stage, density (ρ) has reached its updated value at $(n+1)$th step, while momentum (m_x, m_y) and energy E need to be further advanced due to the non-advection phase.

(ii) Calculate the trajectory averages for all moments by

$$\overline{{}^{V}\phi}^{\bar{\diamondsuit}} = \frac{1}{2}(\overline{{}^{V}\phi}^{n} + \overline{{}^{V}\phi}^{\diamondsuit}) \quad \text{and} \quad \overline{{}^{S^\alpha}\phi}^{\bar{\diamondsuit}} = \frac{1}{2}(\overline{{}^{S^\alpha}\phi}^{n} + \overline{{}^{S^\alpha}\phi}^{\diamondsuit}) \quad \text{for } \alpha = x, y. \tag{51}$$

(iii) With the trajectory averages, compute the viscosity related part to update the VIAs as $\overline{{}^{V}m_x}^{\diamondsuit\diamondsuit}$, $\overline{{}^{V}m_y}^{\diamondsuit\diamondsuit}$ and $\overline{{}^{V}E}^{\diamondsuit\diamondsuit}$ using the corresponding discretized operators in Eqs. (38), (41) and (44). Thus, the time increments of the VIAs due to the viscosity, i.e., $\delta_t^{\diamondsuit\diamondsuit}(\overline{{}^{V}m_x})$, $\delta_t^{\diamondsuit\diamondsuit}(\overline{{}^{V}m_y})$ and $\delta_t^{\diamondsuit\diamondsuit}(\overline{{}^{V}E})$, are known and the SIAs are advanced by the TEC as

$$\overline{{}^{S^\alpha}m_{\beta_{I_\alpha}}}^{\diamondsuit} \overset{\text{TEC}}{\rightarrow} \overline{{}^{S^\alpha}m_{\beta_{I_\alpha}}}^{\diamondsuit\diamondsuit} \quad \text{with } \alpha, \beta = x, y \tag{52}$$

and

$$\overline{{}^{S^\alpha}E_{I_\alpha}}^{\diamondsuit} \overset{\text{TEC}}{\rightarrow} \overline{{}^{S^\alpha}E_{I_\alpha}}^{\diamondsuit\diamondsuit} \quad \text{with } \alpha = x, y. \tag{53}$$

(iv) Compute the intermediate VIA of pressure by

$$\overline{{}^{V}p_{ij}}^{\diamondsuit\diamondsuit} = [\overline{{}^{V}E_{ij}}^{\diamondsuit\diamondsuit} - \overline{{}^{V}\rho_{ij}}^{n+1}(\overline{{}^{V}\mathbf{u}_{ij}}^{\diamondsuit\diamondsuit})^2/2](\gamma - 1), \tag{54}$$

where $\overline{{}^{V}\mathbf{u}}_{ij}^{\diamond\diamond} = \overline{{}^{V}\mathbf{m}}_{ij}^{\diamond\diamond} / \overline{{}^{V}\rho}_{ij}^{n+1}$.

(v) The pressure-based projection is conducted by the following inner loop with a time step $t_s = \Delta t/L$, where L is the number of the iteration of the inner loop.

- Given $\overline{{}^{V}p}_{ij}^{(0)} = \overline{{}^{V}p}_{ij}^{\diamond\diamond}$, $\overline{{}^{S^\alpha}\mathbf{m}}_{I_\alpha}^{(0)} = \overline{{}^{S^\alpha}\mathbf{m}}_{I_\alpha}^{\diamond\diamond}$, $\overline{{}^{V}\mathbf{m}}_{ij}^{(0)} = \overline{{}^{V}\mathbf{m}}_{ij}^{\diamond\diamond}$, $\overline{{}^{S^\alpha}E}_{I_\alpha}^{(0)} = \overline{{}^{S^\alpha}E}_{I_\alpha}^{\diamond\diamond}$, $\overline{{}^{V}E}_{ij}^{(0)} = \overline{{}^{V}E}_{ij}^{\diamond\diamond}$;
- *do* $l = 1, L$
  Solve the following Poisson equation for $\overline{{}^{V}p}_{ij}^{(l)}$

$$\delta_x(\overline{{}^{S^x}\partial_x p}^{(l)})_{ij} + \delta_y(\overline{{}^{S^y}\partial_y p}^{(l)})_{ij} - \frac{1}{(C_{ij}^{(l-1)}\Delta t_s)^2}\overline{{}^{V}p}_{ij}^{(l)} = \frac{1}{\Delta t_s}\left(-\overline{{}^{V}u}_{ij}^{(l-1)}\delta_x(\overline{{}^{S^x}\rho}^{n+1})_{ij} - \overline{{}^{V}v}_{ij}^{(l-1)}\delta_y(\overline{{}^{S^y}\rho}^{n+1})_{ij}. - \frac{1}{(C_{ij}^{(l-1)}\Delta t_s)^2}\overline{{}^{V}p}_{ij}^{(l-1)} + \delta_x(\overline{{}^{S^x}m_x}^{(l-1)})_{ij} + \delta_y(\overline{{}^{S^y}m_y}^{(l-1)})_{ij}\right), \tag{55}$$

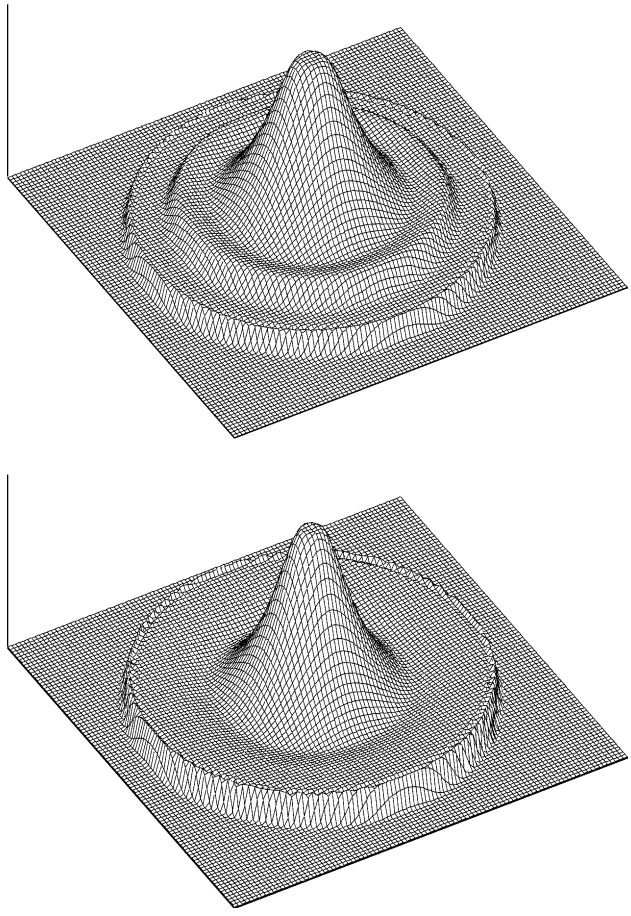

Fig. 2. Bird's eye views of the density (top) and pressure (bottom) of the circular explosion test at $t = 0.25$.

where $C_{ij}^{(l)} = \sqrt{\gamma \overline{{}^{V}p}_{ij}^{(l)} / \overline{{}^{V}\rho}_{ij}^{n+1}}$, and the gradient terms of pressure on the left-hand side of (55) is discretized by using the interpolation approximation (25).

As long as the Poisson equation for the VIA of pressure ($\overline{{}^{V}p}^{(l)}$) is solved, all moments are advanced by

$$\overline{{}^{S^x}m_x}_{i+\frac{1}{2}}^{(l)} = \overline{{}^{S^x}m_x}_{i+\frac{1}{2}}^{(l-1)} - \overline{{}^{S^x}\partial_x p}_{i+\frac{1}{2}}^{(l)} \Delta t_s, \tag{56}$$

$$\overline{{}^{V}m_x}_{ij}^{(l-1)} \overset{\text{TEC}}{\longrightarrow} \overline{{}^{V}m_x}_{ij}^{(l)}, \tag{57}$$

$$\overline{{}^{S^y}m_x}_{ij+\frac{1}{2}}^{(l-1)} \overset{\text{TEC}}{\longrightarrow} \overline{{}^{S^y}m_x}_{ij+\frac{1}{2}}^{(l)}, \tag{58}$$

$$\overline{{}^{S^y}m_y}_{ij+\frac{1}{2}}^{(l)} = \overline{{}^{S^y}m_y}_{ij+\frac{1}{2}}^{(l-1)} - \overline{{}^{S^y}\partial_y p}_{ij+\frac{1}{2}}^{(l)} \Delta t_s, \tag{59}$$

$$\overline{{}^{V}m_y}_{ij}^{(l-1)} \overset{\text{TEC}}{\longrightarrow} \overline{{}^{V}m_y}_{ij}^{(l)}, \tag{60}$$

$$\overline{{}^{S^x}m_y}_{i+\frac{1}{2}j}^{(l-1)} \overset{\text{TEC}}{\longrightarrow} \overline{{}^{S^x}m_y}_{i+\frac{1}{2}j}^{(l)}, \tag{61}$$

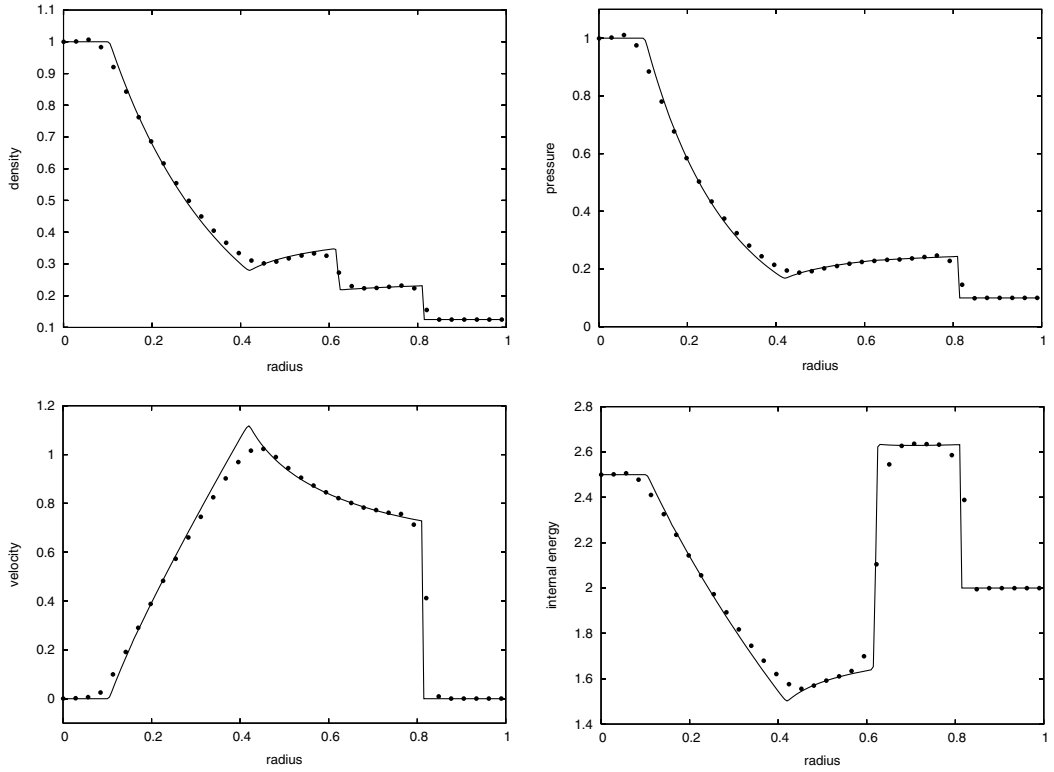

Fig. 3. The profiles of density (top-left), pressure (top-right), velocity (bottom-left) and internal energy (bottom-right) along the line of $x = y$ in the first quadrant. The corresponding 3D views for density and pressure are shown in Fig. 2.

$$\overline{{}^{V}E}_{ij}^{(l)} = \overline{{}^{V}E}_{ij}^{(l-1)} - [\delta_x(\overline{{}^{S^x}up}^{(l)})_{ij} + \delta_y(\overline{{}^{S^y}vp}^{(l)})_{ij}]\Delta t_s, \tag{62}$$

$$\overline{{}^{S^\alpha}E}_{I_\alpha}^{(l-1)} \overset{\text{TEC}}{\rightarrow} \overline{{}^{S^\alpha}E}_{I_\alpha}^{(l)} \quad \text{with } \alpha = x, y, \tag{63}$$

$$\overline{{}^{V}p}_{ij}^{(l)} = [\overline{{}^{V}E}_{ij}^{(l)} - \overline{{}^{V}\rho}_{ij}^{n+1}(\overline{{}^{V}\mathbf{u}}_{ij}^{(l)})^2/2](\gamma - 1). \tag{64}$$

end do

(vi) Update momentum and energy as $\overline{{}^{S^\alpha}\mathbf{m}}_{I_\alpha}^{n+1} = \overline{{}^{S^\alpha}\mathbf{m}}_{I_\alpha}^{(L)}$, $\overline{{}^{V}\mathbf{m}}_{ij}^{n+1} = \overline{{}^{V}\mathbf{m}}_{ij}^{(L)}$, $\overline{{}^{S^\alpha}E}_{I_\alpha}^{n+1} = \overline{{}^{S^\alpha}E}_{I_\alpha}^{(L)}$, $\overline{{}^{V}E}_{ij}^{n+1} = \overline{{}^{V}E}_{ij}^{(L)}$ with $\alpha = x, y$.

(vii) Go to next step.

We should note that the inner loop with a smaller time step interval is not necessary for computational stability, but for a more accurate solution to the rarefaction wave when a relatively large CFL number is used. Renewing pressure by (64) in the inner loop does not make noticeable difference in the numerical solution and is not used in low Mach flows.

In (57) and (60), the VIAs of momentum are computed by TEC formula after the SIAs of the components normal to the surface elements in respective directions are corrected by pressure gradient force. We should note that the coupling between pressure and velocity in the projection step is computed through the VIA of the pressure and the SIA of the normal components of velocity. Considering that the VIA and the SIA are staggeringly located, the pressure and the velocity are well linked. Since we

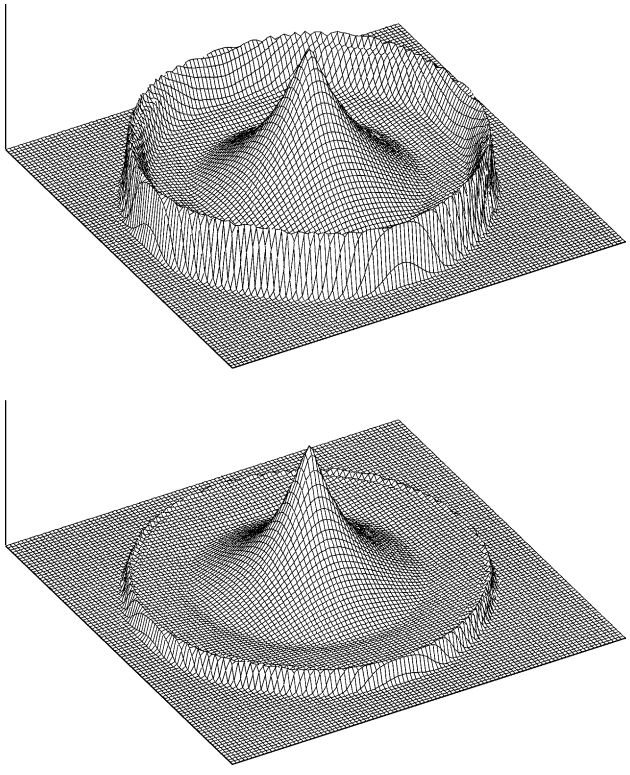

Fig. 4. Same as Fig. 2, but with the initial pressure in the center region being 10. The output is at $t = 0.095$.

use both VIA and SIA as the model variables, the spatial discretization in VSIAM3 can be constructed in a more natural way, where the poor pressure–velocity coupling in the collocated grid and the averaging across different control volume in the conventional staggered grid are circumvented. Thus, VSIAM3 gives a more robust and accurate spatial discretization for finite volume methods that use pressure projection approach.

3. Numerical examples

Two types numerical tests were carried out to verify the proposed method. The first includes 2D explosion and implosion of inviscid compressible flows to test the method as a solver for compressible flows that contain shock waves. Another one is the lid driven cavity flow of viscous fluid [4] to show the capability of the method in computing low Mach or incompressible flows.

3.1. 2D explosion tests

A symmetric two-dimensional explosion, which is reported in [18], on the computational domain $[-1,1]\times[-1,1]$ is generated from the following initial condition:

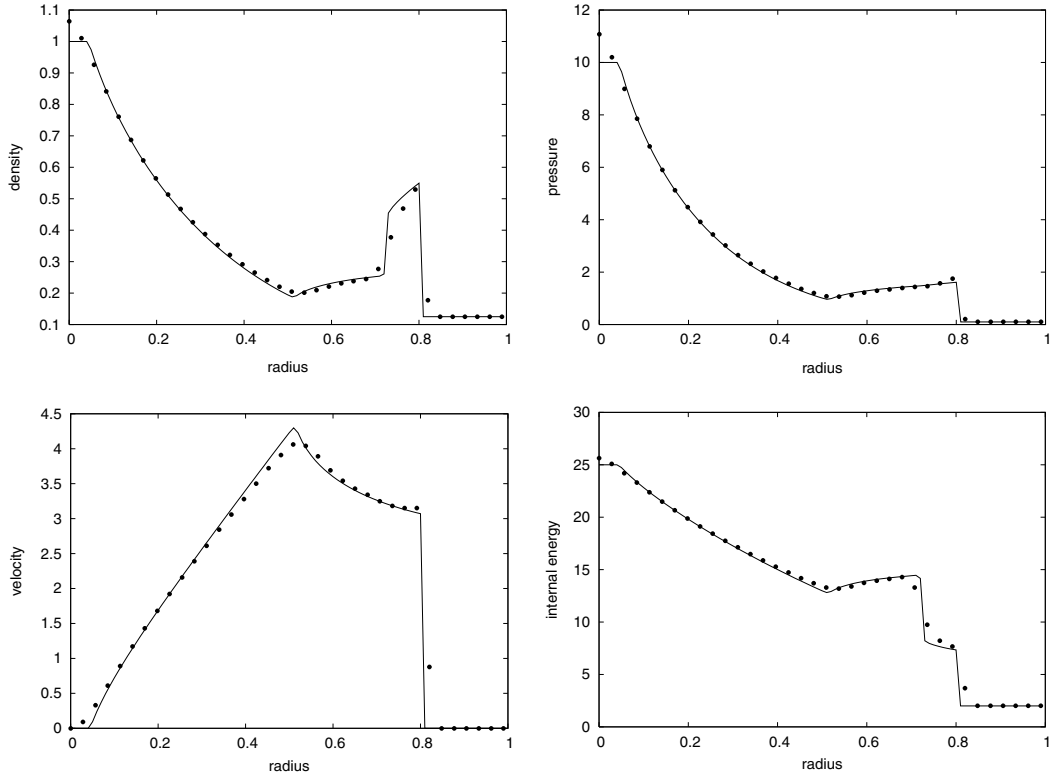

Fig. 5. The profiles of density (top-left), pressure (top-right), velocity (bottom-left) and internal energy (bottom-right) along the line of $x = y$ in the first quadrant. The corresponding 3D views for density and pressure are shown in Fig. 4.

$$(\rho, m_x, m_y, p) = \begin{cases} (1,0,0,1) & \text{for } r \leqslant 0.4, \\ (0.125,0,0,0.1) & \text{for } r > 0.4, \end{cases} \tag{65}$$

where $r = \sqrt{x^2 + y^2}$ is the radius.

The inviscid Euler conservation laws are solved on a 100×100 grid. The time stepping interval is $0.25\Delta/C_0$ with Δ being the mesh spacing and $C_0 = \sqrt{\gamma p_{0c}/\rho_{0c}}$, where p_{0c} and ρ_{0c} are the initial pressure and density in the central region. The number of the inner iteration listed from (55) to (64) is two in the present calculations.

The initial condition (65) produces an axis-symmetric configuration that contains circular out-going shock wave and contact discontinuity and a rarefaction wave expanding inward. The bird's eye views of the density and the pressure at $t = 0.25$ are displayed in Fig. 2. The axis-symmetric solution is accurately reproduced on a Cartesian grid. Shock wave, contact discontinuity and rarefaction fan are well resolved.

In order to verify our 2D computations, we make use of the symmetry and reduce the axis-symmetric Euler equations to the following 1D system in the radius direction with source terms that reflect the geometric effects

$$\frac{\partial \mathbf{U}}{\partial t} + \frac{\partial \mathbf{F}(\mathbf{U})}{\partial r} = \mathbf{S}(\mathbf{U}), \tag{66}$$

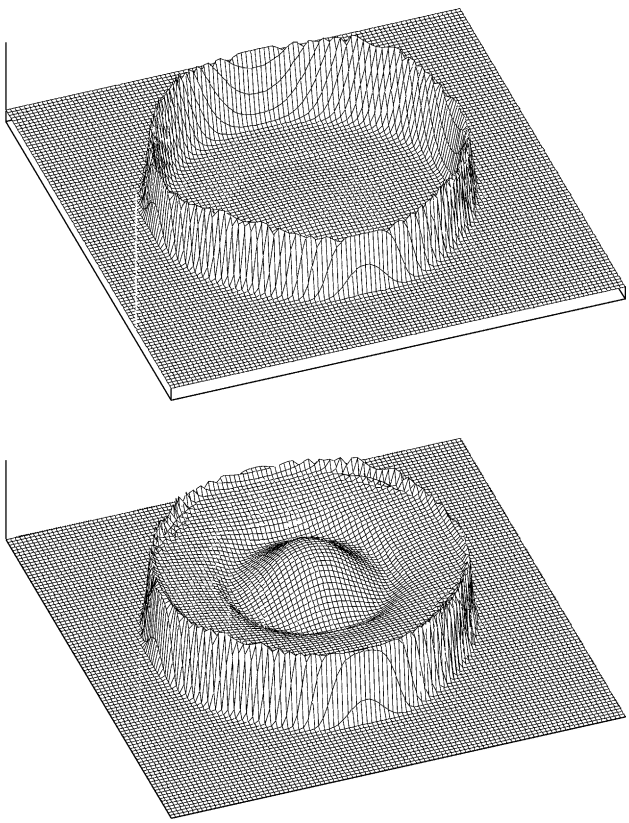

Fig. 6. Same as Fig. 2, but for the initial conditions given by (67). The output is at $t = 0.00012$.

where

$$\mathbf{U} = \begin{pmatrix} \rho \\ m \\ E \end{pmatrix},$$

$$\mathbf{F}(\mathbf{U}) = \begin{pmatrix} m \\ um + p \\ Eu + pu \end{pmatrix}$$

and

$$\mathbf{S}(\mathbf{U}) = -\frac{1}{r}\begin{pmatrix} m \\ um \\ Eu + pu \end{pmatrix},$$

where u is the radial velocity and $m = \rho u$.

The reference solutions are obtained by solving (66) with the one-dimensional code of VSIAM3 [24] on a fine mesh (20,000 cells). Indicated by the solid lines in Fig. 3, the reference solutions are visually identical to those given in [18].

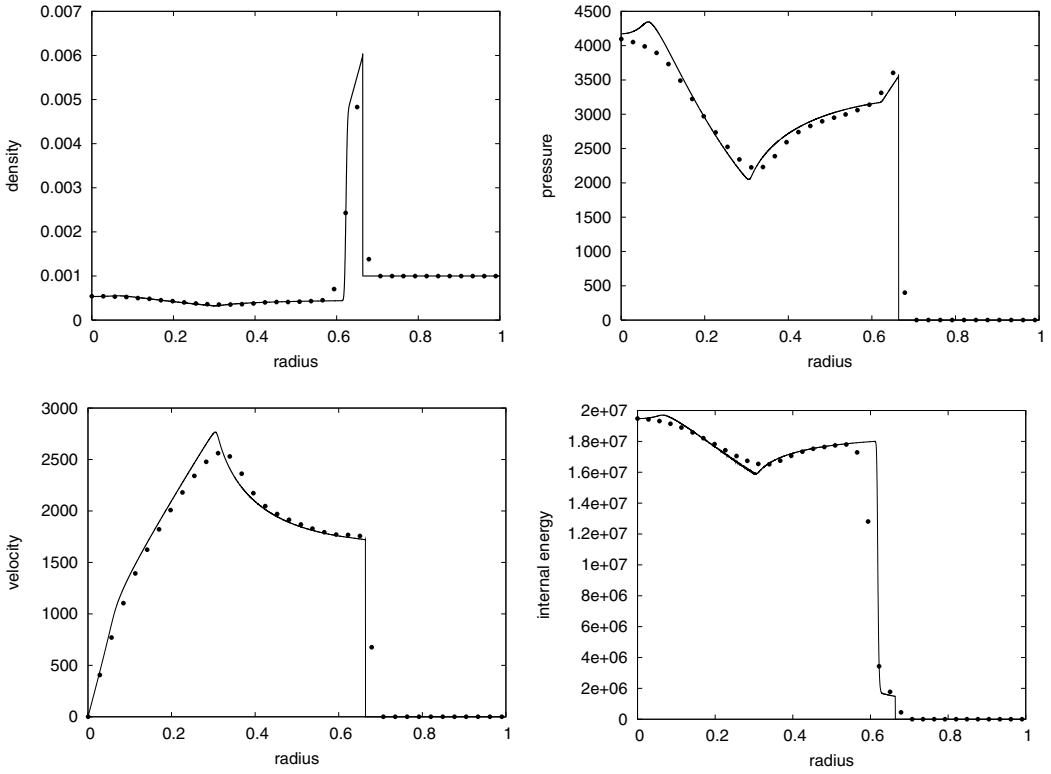

Fig. 7. The profiles of density (top-left), pressure (top-right), velocity (bottom-left) and internal energy (bottom-right) along the line of $x = y$ in the first quadrant. The corresponding 3D views for density and pressure are shown in Fig. 6.

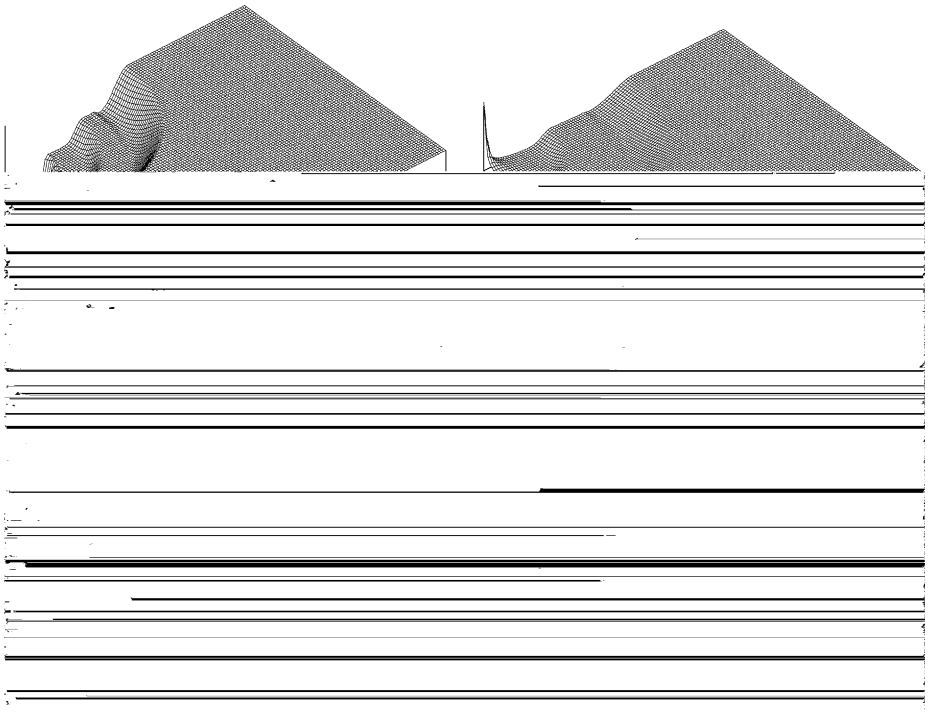

Fig. 8. Bird's eye views of the density evolution of the cylindrical implosion test. Displayed are the outputs at $t = 0.0855$ (top-left), 0.1475 (top-right), 0.1933 (bottom-left) and 0.2896 (bottom-right) in the first quadrant.

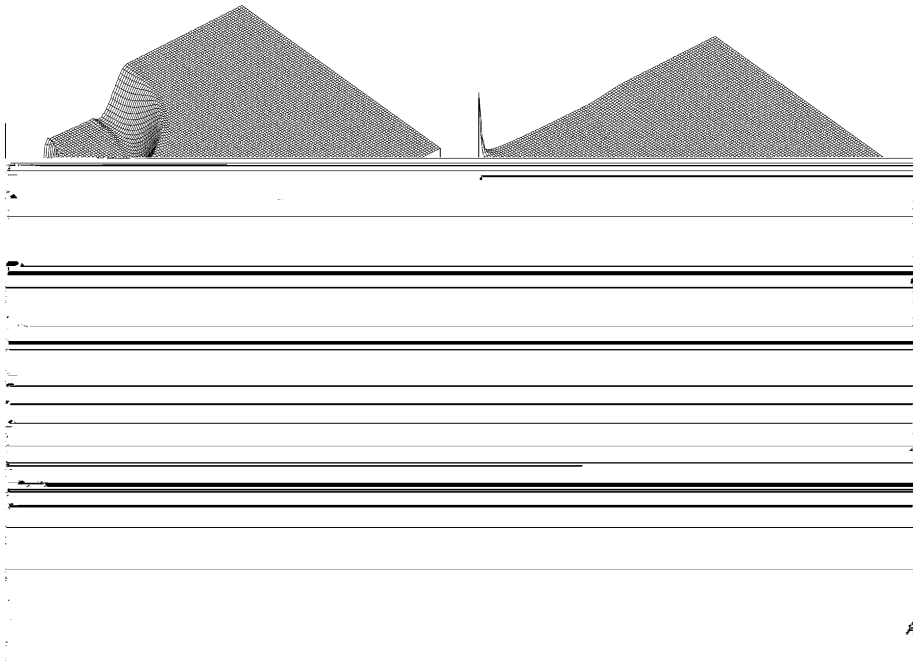

Fig. 9. Same as Fig. 8, but for pressure field.

Plotted in Fig. 3 are the profiles of density, pressure, velocity and internal energy along the cross-section of $x = y$ against the reference solutions at $t = 0.25$. The numerical solutions of the proposed method agree well with the reference solutions even with a coarse computational mesh. Both the shock and the contact discontinuity are accurately computed with compact thickness. The rarefaction wave is also well simulated.

We increased the central pressure to 10 and ran the test up to $t = 0.095$. The 3D views of density and pressure are shown in Fig. 4. Impelled by the higher pressure, the shock wave is more than doubly strengthened, and a thin compressed layer develops between the shock and the contact discontinuity. Again, the cylindrical shock front is accurately simulated. The physical variables along $x = y$ are plotted in Fig. 5, where shock and contact discontinuity are well resolved. The circular front of the expansion fan converges at the center. The numerical diffusion in velocity causes an overshot when the expansion fan collides.

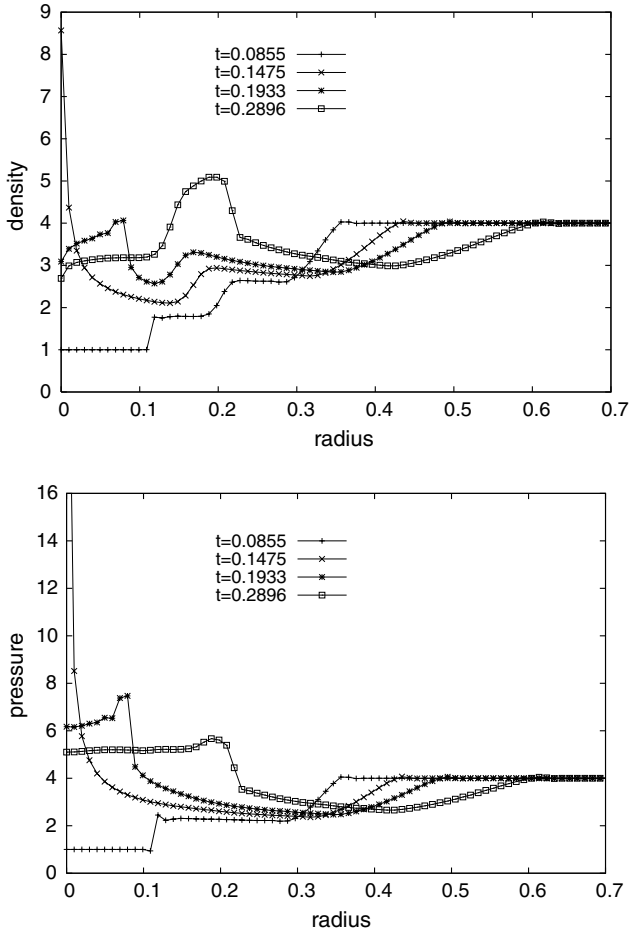

Fig. 10. Density (top) and pressure (bottom) profiles at different instants along the line of $x = y$ in the first quadrant for the cylindrical implosion test. The corresponding 3D views are shown in Figs. 8 and 9.

An explosion in a low Mach flow is computed with the initial condition defined by

$$(\rho, m_x, m_y, p) = \begin{cases} (10^{-3}, 0, 0, 1^4) & \text{for } r \leqslant 0.4, \\ (10^{-3}, 0, 0, 1^{-1}) & \text{for } r > 0.4. \end{cases} \tag{67}$$

The maximum Mach number in this case is less than 0.01 because of low density. There are, however, very large jumps in pressure, velocity and internal energy across the right moving shock wave. As shown in Fig. 6, the presented method gives axis-symmetrical results where the high density region between the shock and the contact discontinuity with a thickness less than 5 mesh cells is adequately reproduced. From Fig. 7, it is observed that the shock is well resolved with a correct displacement even a small overshot in pressure occurs right behind the shock wave. Similar to the previous test, the expansion region looks a little bit diffused. We find that some improvements in the numerical accuracy for expansion wave can be achieved by properly adjusting the sub-circle of the computations for acoustic waves. The structure of the whole system has been sufficiently simulated even with a low resolution grid.

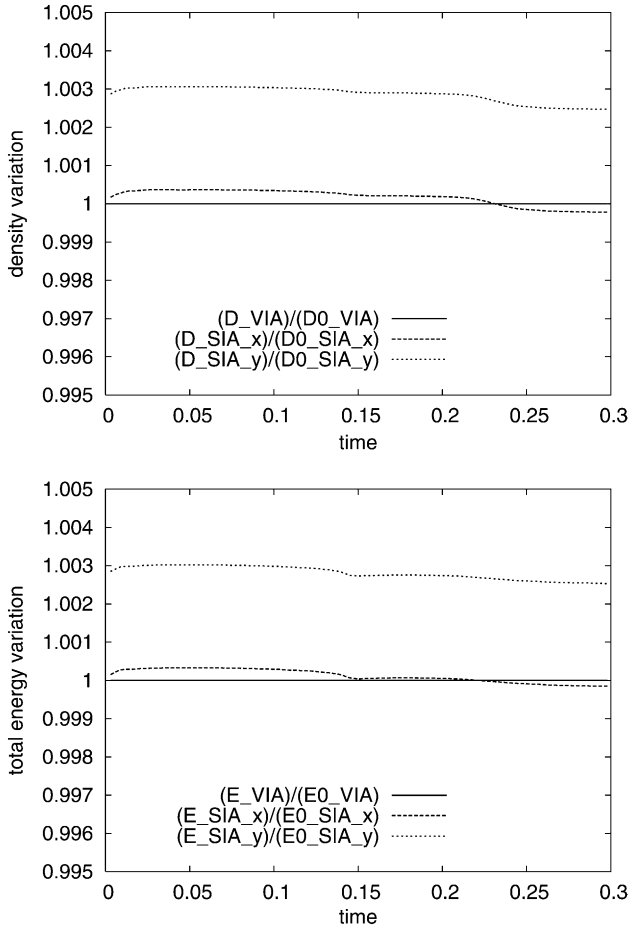

Fig. 11. The variation in the density (top) and the total energy (bottom) integrated over the whole computational domain. Displayed are the ratio of the computed density at different instants against the initial density. The shown quantities are defined as D0_SIA_x $= \sum \overline{S^x \rho(0)}$, D0_SIA_y $= \sum \overline{S^y \rho(0)}$, D0_VIA $= \sum \overline{V \rho(0)}$, D_SIA_x $= \sum \overline{S^x \rho(t)}$, D_SIA_y $= \sum \overline{S^y \rho(t)}$, D_VIA $= \sum \overline{V \rho(t)}$ and E0_SIA_x $= \sum S^x \rho(0)$, E0_SIA_y $= \sum S^y \rho(0)$, E0_VIA $= \sum V \rho(0)$, E_SIA_x $= \sum S^x \rho(t)$, E_SIA_y $= \sum S^y \rho(t)$, E_VIA $= \sum V \rho(t)$.

3.2. 2D implosion test

Cylindrical implosion has been numerically studied by using some 1D schemes for the reduced axis-symmetrical Euler equations (66) in [17,14]. Equivalently, we conducted a fully two-dimensional computation with the following initial condition:

$$(\rho, m_x, m_y, p) = \begin{cases} (1,0,0,1) & \text{for } r \leqslant 0.4, \\ (4,0,0,4) & \text{for } r > 0.25. \end{cases} \tag{68}$$

Contrary to explosion, an inward shock and contact discontinuity converge toward the center. According to the previous studies [17,14], the converging circular shock collides, and a high pressure and high density region is generated at the domain center. The reflected shock will then move outward and interacts with the inward moving contact discontinuity. The interactions among various waves make the process very complex, but the axis-symmetry should remain through the whole process. This problem provides a

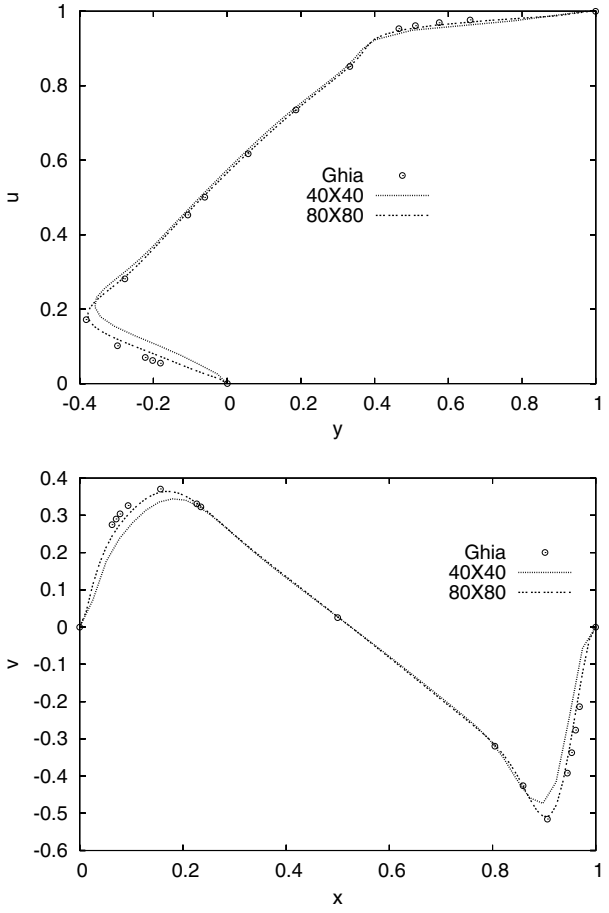

Fig. 12. The x component (top) and the y component (bottom) of the velocity of nearly incompressible viscous flow with the Mach number being 8.4×10^{-5} and the Reynolds number being 1000. Displayed are the results on 40×40 and 80×80 meshes against the result in [4].

Table 1
Conditions for lid driven viscous cavity flows

	Pressure	Density	Mach No.
Case 1	4×10^{-1}	1	1.3
Case 2	4	1	0.42
Case 3	4×10^{1}	1	0.13
Case 4	4×10^{2}	1	0.042

challenging test bed to multi-dimensional codes for their accuracy and grid dependency. Any systematic discrepancy will drive the configuration away from the circular symmetry, especially in the later stage after converging shock collides and reflected from the origin.

We used a 200×200 grid on a $[-0.7,0.7]\times[-0.7,0.7]$ computational domain, which is still a low resolution compared to those reported in 1D computations for the reduced axis-symmetric system. 3D views of density and pressure at different instants are shown in Figs. 8 and 9. As expected, the converging shock creates a sharp pulse of high density and high pressure at the center, which then causes an explosion moving outward in an axis-symmetry. Our 2D simulation reproduced the cylindrical configuration. More detailed examinations were carried out by plotting the cross-section profile of density and pressure along $x=y$ in a way similar to [14] in Fig. 10. Compared with the corresponding figures in [14] (i.e., Figs. 6(a) and (c) therein), our numerical results agree well with the 1D axis-symmetric simulation. All the shocks (including the inward shock and the reflected shock), contact discontinuity and the rarefaction wave are adequately resolved even with fewer computational grid. The second shock as mentioned in [14], however, cannot be clearly identified in the present simulation probably because of the low spatial resolution of the computational grid.

We examined the conservation by summing up the density and the total energy over the whole computational domain. The variations of the density and the total energy in respect to their initial values of the whole system are plotted against the time in Fig. 11. The VIAs of density and total energy are exactly conserved, while the SIA quantities experience small change of an order less than 0.3%.

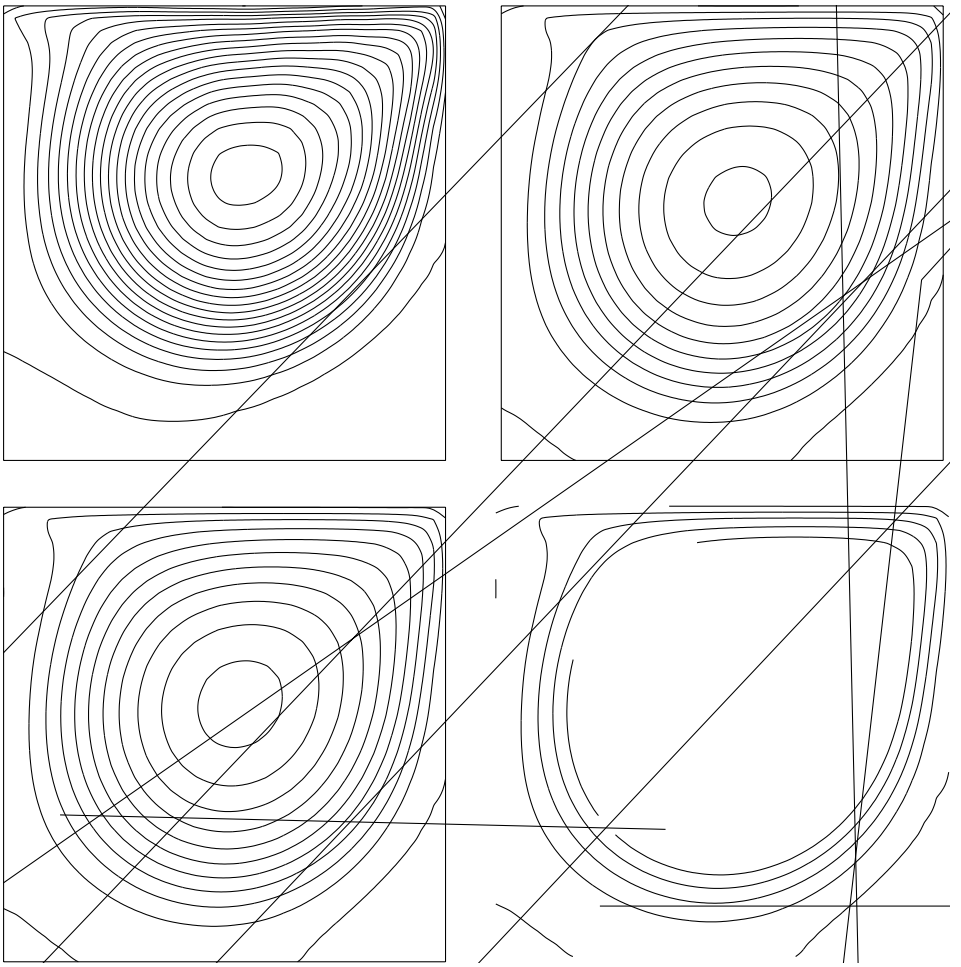

3.3. Lid driven cavity flows

To evaluate the presented method in simulations of low Mach or nearly incompressible viscous flows, we computed the widely used benchmark test of the lid driven cavity flow [4]. We still use the equation of state of ideal gas. The initial density is unity for all the cases reported in this paper. The compressibility of the flow is controlled by choosing different pressure. A nearly incompressible flow is approximated by setting $p = 10^8$, thus the corresponding Mach number is 8.4×10^{-5}. Simulations with a Reynolds number of 1000 is conducted on 40×40 and 80×80 grids. The CFL number is 0.35 in terms of the driving velocity of the upper lid ($u = 1$) and independent of the sound speed. The computation is stable no matter how large the sound speed is. The horizontal velocity component u along the $x = 0.5$ axis and the v component along the $y = 0.5$ axis are plotted in Fig. 12. It is observed that the result of 80×80 grid computation is in good agreement with [4], and the simulation on a 40×40 grid also gives an adequate result. Fig. 13 shows the stream function of the steady solution on a 80×80 grid. The typical flow patterns are accurately captured.

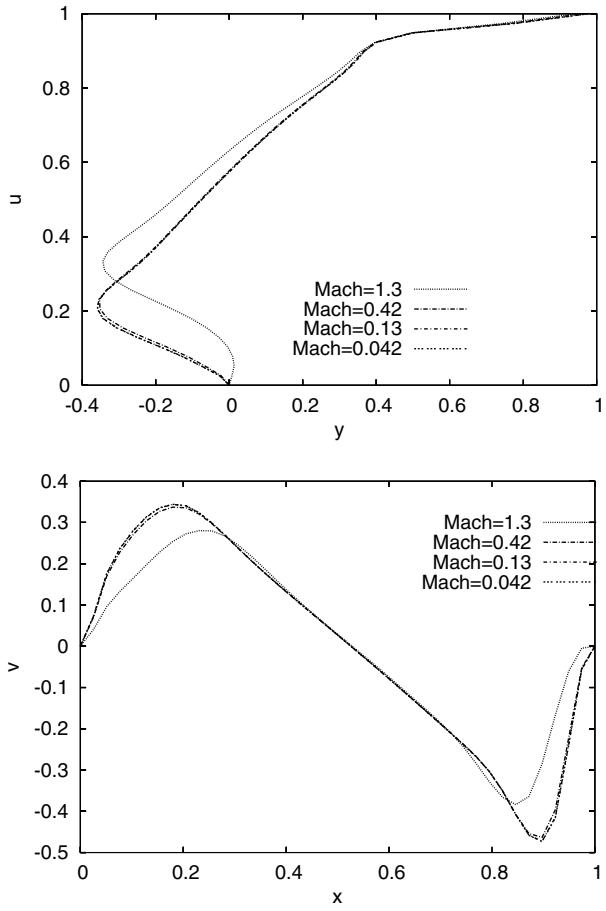

Fig. 15. The x component (top) and the y component (bottom) of the velocities of the cavity flows of different Mach numbers.

It is revealed that the proposed method works well in the limit of incompressible flow and is able to give accurate solutions to incompressible flows.

It is also interesting to see how the compressibility affects the development of the cavity flow. We carried out a series experiments with the initial conditions given in Table 1. A grid of 40×40 and a CFL of 0.35 are used for all cases. The stream lines at $t = 25$ for all cases are displayed in Fig. 14. The corresponding profiles of u and v along the center lines are plotted in Fig. 15. The result of case 1, which never reaches a steady state, is significantly different from the other three. The results of case 3 and case 4 are visually identical to the nearly incompressible result in Fig. 12. In order to examine the evolutions of the cavity flows in all cases, we show the minimum value of the stream function and the position of the primary vortex as a function of time in Figs. 16 and 17. Case 1 is characterized by a significant compressibility which causes the oscillation in the strength of the primary vortex. The position of the primary vortex center in case 1 moves along a spiral like trail and is closer to the upper moving boundary compared to other cases. Case 2 has also oscillations in the development of the vortex, while the vortex center move in a course more similar to the less compressible cases. In the low Mach or less compressible cases (cases 3 and 4), the primary vortex is monotonically strengthened and moves to its final position in a much stable way. It is found that cases 3 and 4 do not make

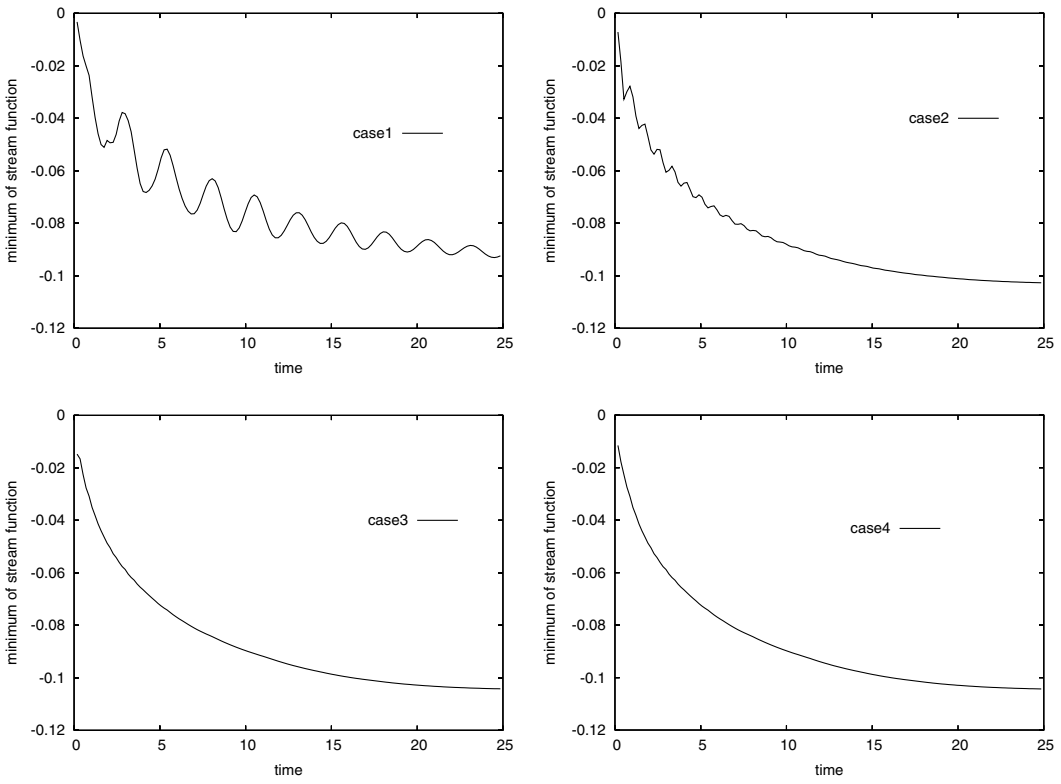

Fig. 16. The strength development of the primary vortex in different Mach flows. See Table 1 for the condition for each case.

noticeable difference. We may conclude that for steady incompressible viscous flows, a flow of a Mach number less than 0.1 can be reasonably used to model a completely incompressible flow.

4. Conclusions

We have presented a multi-dimensional formulation for flows of any Mach number. A fractional step solution procedure, where pressure is used as an auxiliary variable and updated by a semi-implicit manner, is combined with the VSIAM3, a CIP/multi-moment finite volume method. With two kinds of integrated moments, i.e., VIA and SIA, a multi-dimensional spatial discretization is constructed and well suited to the pressure-based projection algorithm. The VIAs is exactly conserved in the computations. Different from the conventional finite volume method, the VSIAM3 does not need the averaging of the velocity variables onto the staggered grid point for advection computation in a staggered mesh, nor the extra treatment for the poor pressure–velocity link in a collocated mesh. Hence, the solver appears to be more robust and accurate. Geometrically faithful solution with less effects of the grid system can then be obtained.

The proposed method has been verified with typical multi-dimensional tests for compressible and less compressible flows. Numerical results show that the present method is a conservative, robust and adequately accurate solver for all Mach number flows.

With its multi-dimensional version given and validated in this paper, we can expect the present method to be practical in many applications.

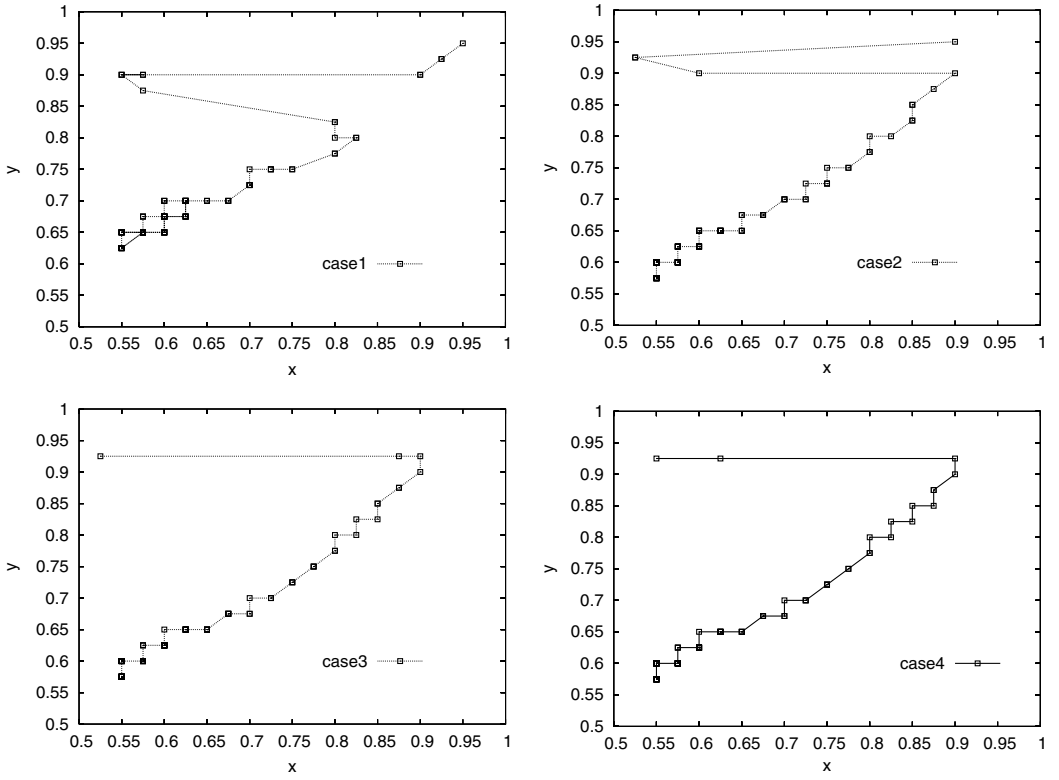

Fig. 17. The displacement of the center position of the primary vortex as a function of time. The uppermost point indicates the start point of the primary vortex.

Acknowledgments

The authors gratefully acknowledge the discussions with Prof. T. Yabe and the constructive comments of the anonymous referees. This work is supported in part by the Grant-in-Aid for scientific research of Japan Society for the Promotion of Science (No. 16605002).

References

[1] H. Bijl, P. Wesseling, A unified method for computing incompressible and compressible flows in boundary-fitted coordinates, J. Comput. Phys. 141 (1998) 153.
[2] A. Clappier, A correction method for use in multidimensional time-splitting advection algorithms: application to two- and three-dimensional transport, Mon. Weather Rev. 126 (1998) 223.
[3] A. Chorin, Numerical solution of the Navier–Stokes equations, Math. Comput. 22 (1968) 745.
[4] U.K. Ghia, N. Ghia, C.T. Shin, High-Re solution for incompressible flow using the Navier–Stokes equations end a multi-grid method, J. Comput. Phys. 48 (1982) 387.
[5] H. Guillard, C. Viozat, On the behavior of upwind schemes in the low Mach number limit, Comput. Fluids 28 (1999) 63.
[6] F. Harlow, E. Welch, Numerical calculation of time-dependent viscous incompressible flow of fluid with a free surface, Phys. Fluids 8 (1965) 2182.
[7] F. Harlow, A. Amsden, Numerical calculation of almost incompressible flows, J. Comput. Phys. 3 (1968) 80.
[8] F. Harlow, A. Amsden, A numerical fluid dynamics calculation method for all flow speeds, J. Comput. Phys. 8 (1971) 197.

[9] R. Issa, Solution of the implicitly discretized fluid flow equations by operator-splitting, J. Comput. Phys. 62 (1986) 40.
[10] R. Issa, D. Gosman, A. Watkins, The computation of compressible and incompressible flows by a non-iterative implicit scheme, J. Comput. Phys. 62 (1986) 66.
[11] C. Karki, S. Patankar, Pressure based calculation procedure for viscous flows at all speed in arbitrary configurations, AIAA J. 27 (1989) 1167.
[12] J. Kim, P. Moin, Application of a fractional step method to incompressible Navier–Stokes equations, J. Comput. Phys. 59 (1985) 308.
[13] B. Koren, B. van Leer, Analysis of preconditioning and multi-grid for Euler flows with low-subsonic regions, Adv. Comput. Meth. 4 (1995) 127–144.
[14] T.G. Liu, B.C. Khoo, K.S. Yeo, The numerical simulations of explosion and implosion in air: use of a modified Harten's TVD scheme, Int. J. Numer. Meth. Fluid 31 (1999) 661.
[15] J. McGuirk, J. Page, Shock capturing using a pressure correction method, AIAA J. 28 (1990) 1751.
[16] W. Shyy, E. Braaten, Adaptive grid computation for inviscid compressible flows using a pressure correction method, AIAA Paper 88-3566, 1988.
[17] G.A. Sod, A numerical study of a converging cylindrical shock, J. Fluid Mech. 83 (1977) 785.
[18] E. Toro, Riemann Solvers and Numerical Methods for Fluid Dynamics, Springer, Berlin, 1997.
[19] E. Turkel, Review of preconditioning techniques for fluid dynamics, Appl. Numer. Math. 21 (1993) 257.
[20] E. Turkel, R. Radespiel, H. Kroll, Assessment of preconditioning methods for multidimensional aerodynamics, Comput. Fluids 26 (1997) 613.
[21] D.R. van der Heul, C. Vuik, P. Wesseling, A conservative pressure-correction method for flow at all speeds, Comput. Fluids 32 (2003) 1113.
[22] M. Weiss, A. Smith, Preconditioning applied to variable and constant density flows, AIAA J. 22 (1995) 745.
[23] P. Wesseling, Principles of Computational Fluid Dynamics, Springer, Berlin, 2000.
[24] F. Xiao, Unified formulation for compressible and incompressible flows by using multi integrated moments I: one-dimensional inviscid compressible flow, J. Comput. Phys. 195 (2004) 629.
[25] F. Xiao, A. Ikebata, T. Hasegawa, Numerical simulations of free-interface fluids by a multi integrated moment method, Comput. Struct. 83 (2005) 409.
[26] F. Xiao, T. Yabe, Completely conservative and oscillation-less semi-Lagrangian schemes for advection transportation, J. Comput. Phys. 170 (2001) 498.
[27] F. Xiao, T. Yabe, X. Peng, H. Kobayashi, Conservation and oscillation-less transport schemes based on rational functions, J. Geohys. Res. 107 (2002) 4609.
[28] T. Yabe, T. Aoki, A universal solver for hyperbolic-equations by cubic-polynomial interpolation. 1. One-dimensional solver, Comput. Phys. Commun. 66 (1991) 219.
[29] T. Yabe, R. Tanaka, T. Nakamura, F. Xiao, Exactly conservative semi-Lagrangian scheme (CIP-CSL) in one dimensionm, Mon. Weather Rev. 129 (2001) 332.
[30] T. Yabe, P. Wang, Unified numerical procedure for compressible and incompressible fluid, J. Phys. Soc. Jpn. 60 (1991) 2105.
[31] T. Yabe, F. Xiao, T. Utsumi, The constrained interpolation profile method for multiphase analysis, J. Comput. Phys. 169 (2001) 556.